Polarization encoding as a novel approach to MRI

Jaakko O. Nieminen [a,b,*], Martin Burghoff [b], Lutz Trahms [b], Risto J. Ilmoniemi [a]

[a] Helsinki University of Technology, Department of Biomedical Engineering and Computational Science, P.O. Box 2200, FI-02015 TKK, Finland
[b] Physikalisch-Technische Bundesanstalt (PTB), Abbestr. 2-12, 10587 Berlin, Germany

ABSTRACT

In magnetic resonance imaging (MRI), there have been three basic techniques to encode the spatial origin of the signals, i.e. Fourier and radio frequency encoding and the use of sensitivity information of sensor arrays. In this paper, we introduce a new encoding method, which we call polarization encoding. The method utilizes sets of polarizing fields with various spatial profiles; it is tailored for MRI at ultra-low fields (ULF MRI). In ULF MRI, signals from a prepolarized sample are typically detected using an array of SQUID (superconducting quantum interference device) sensors at microtesla fields. The prepolarization is achieved with a field of the order of 10–100 mT preceding the signal acquisition. In polarization encoding, the prepolarizing field is varied in a way to gain additional information about the sample. The method may also prove useful for modalities that in the absence of any precession aim to image the DC magnetization profile of a sample.

© 2009 Elsevier Inc. All rights reserved.

1. Introduction

Magnetic resonance imaging (MRI) was made possible by the introduction of methods that encode the spatial origin of the nuclear magnetic precession signals. In Fourier encoding, linear magnetic field gradients are applied during or prior to the signal acquisition [1]; as a result, the phase and the frequency of the precession signal depend linearly on its spatial position; the image can be reconstructed via inverse Fourier transform. Commonly, Fourier encoding methods require slice selection to reduce the signal dimension. In contrast, radio-frequency (RF) encoding uses RF pulses to produce spatial magnetization profiles [2–4]; for example, sample magnetization can be tilted with suitable RF pulses to produce wavelet-shaped signal profiles and the image reconstruction is achieved via an inverse wavelet transform.

Parallel imaging techniques (pMRI), e.g. SMASH, SENSE, or GRAPPA [5–7], have offered a significant increase in imaging speed. In pMRI, signals are received with a sensor array and the spatially varying sensitivity profiles of the sensors are used for signal encoding. When imaging with K sensors, imaging times can be at most K times reduced in comparison to single-sensor imaging; in practice, such high a reduction is unreachable.

Recently, several research groups have started to develop ultra-low-field MRI (ULF MRI) [8–10]. In ULF MRI, precession signals are detected typically at microtesla fields using highly sensitive sensors, such as superconducting quantum interference devices (SQUIDs) [8], giant magnetoresistance (GMR) sensors [11,12], or atomic magnetometers [13]. Because signals in ULF MRI are recorded at fields orders of magnitude below the conventional MRI field strength of a few tesla, the detection period is preceded by polarizing the sample at a field of the order of 10 or 100 mT. Despite the prepolarization and highly sensitive sensors, imaging times in ULF MRI tend to be long; therefore, methods to reduce acquisition times are needed. For example, pMRI has been demonstrated to reduce imaging times in ULF MRI [14].

In this paper, we introduce a new encoding method, which we call polarization encoding [15,16]. The encoding protocol includes a series of polarizing fields with various spatial profiles. At this stage, we present only numerical simulations that illustrate the concept. From the technical point of view, the experimental realization seems especially suitable for prepolarization-enhanced ULF MRI. However, it may also prove useful for imaging modalities that in the absence of precession aim to detect directly the DC magnetization profile of a sample.

2. Theory

In MRI, the real-valued signal of a single sensor in the laboratory frame may be expressed as

$$s(t) = \int \mathscr{A}(\mathbf{r}) \cdot \mathscr{M}(\mathbf{r}, t) \mathrm{d}V, \qquad (1)$$

where t is time, $\mathbf{r}$ is the spatial position, $\mathscr{A}(\mathbf{r})$ is the three-component real-valued sensitivity vector of the sensor and $\mathscr{M}(\mathbf{r}, t)$ is the

magnetization vector of the sample at $\boldsymbol{r}$ at time t; the integration is performed over the sample. For numerical analysis, this equation is discretized such that

$$s(t) = \boldsymbol{a} \cdot \boldsymbol{m}(t), \tag{2}$$

where $\boldsymbol{a}$ and $\boldsymbol{m}$ are, in general, $3N_v$-component vectors containing the sensor sensitivities and the magnetization integrals over the N_v voxels.

MRI signals detected by a sensor array can be written in vector form:

$$\boldsymbol{s}(t) = \mathbf{A}\boldsymbol{m}(t), \tag{3}$$

where $\mathbf{A}$ is a sensitivity matrix and $\boldsymbol{m}(t)$ contains the cartesian components of the magnetization vector in each voxel; here, for simplicity, noise is ignored. Let us consider $\mathbf{A}$ in more detail. The lth row of $\mathbf{A}$ contains the sensitivity vector of the lth sensor. If we assume that only the x and y components of the magnetization are detected, $\boldsymbol{m}$ has $2N_v$ elements and $\mathbf{A}$ is an $N_s \times 2N_v$ matrix, where N_s is the number of sensors. The assumption is valid, e.g. when the precession is around the z axis and T_1 relaxation is slow. The evolution of $\boldsymbol{m}$ is governed by the Bloch equations [17].

Eq. (3) allows us to solve only N_s elements of $\boldsymbol{m}$. To obtain additional information about $\boldsymbol{m}$, $\mathbf{A}$ has to be enlarged; polarization encoding allows this. In this method, various polarizing fields are used to magnetize the sample in consecutive measurements. The resulting magnetization depends linearly on the polarizing field. As will be shown, the effect of polarization encoding can be understood using the concept of independent virtual sensors.

Assume that K consecutive measurements are performed such that during the kth acquisition the magnetization is

$$\boldsymbol{m}^{(k)}(t) = \mathbf{C}^{(k)}\boldsymbol{m}(t). \tag{4}$$

In Eq. (4), $\mathbf{C}^{(k)}$ is a block-diagonal conversion matrix, which depends on the kth polarizing field and will be considered below, and $\boldsymbol{m}(0)$ is the magnetization that would be produced by a homogenous polarizing field $\boldsymbol{B}_p = B_p \boldsymbol{e}_x$. The waveforms of the components of $\boldsymbol{m}^{(k)}$ are identical at different trials because, after polarization, they evolve in the same measurement field. Combining Eqs. (3 and 4), the kth measurement records

$$\boldsymbol{s}^{(k)}(t) = \mathbf{A}\mathbf{C}^{(k)}\boldsymbol{m}(t). \tag{5}$$

A composite signal vector $\boldsymbol{s}'$ and a composite sensitivity matrix $\mathbf{A}'$ can be constructed from the $\boldsymbol{s}^{(k)}$:s and $\mathbf{A}\mathbf{C}^{(k)}$:s, respectively:

$$\boldsymbol{s}'(t) = \begin{pmatrix} \boldsymbol{s}^{(1)}(t) \\ \vdots \\ \boldsymbol{s}^{(K)}(t) \end{pmatrix} \quad \text{and} \quad \mathbf{A}' = \begin{pmatrix} \mathbf{A}\mathbf{C}^{(1)} \\ \vdots \\ \mathbf{A}\mathbf{C}^{(K)} \end{pmatrix}. \tag{6}$$

Then,

$$\boldsymbol{s}'(t) = \mathbf{A}'\boldsymbol{m}(t). \tag{7}$$

The elements of $\boldsymbol{s}'$ can be considered to be signals of virtual sensors whose sensitivities are described by the $\mathbf{A}\mathbf{C}^{(k)}$:s. If the polarizing fields are chosen properly,

$$\text{rank } \mathbf{A}' = K \text{ rank } \mathbf{A}, \tag{8}$$

i.e. the number of linearly independent sensors becomes K-fold; this allows us to solve a larger $\boldsymbol{m}$ than with only one polarizing field.

In the following, a general form of the conversion matrices is presented. Assume that the measurement field is $\boldsymbol{B}_m(\boldsymbol{r}, t) = B_m(\boldsymbol{r}, t)\boldsymbol{e}_z$, where $\boldsymbol{r}$ is the spatial position. The time-dependent form of $\boldsymbol{B}_m$ may include encoding gradients, e.g. when polarization encoding is combined with Fourier encoding. During the kth polarization, the polarizing field is $\boldsymbol{B}_p^{(k)}(\boldsymbol{r})$. With this field, the signals follow Eq. (5). Suppose that the $(2i-1)$th and the

$(2i)$th elements of $\boldsymbol{m}(t)$ are the x and y components of the magnetization at $\boldsymbol{r}_i$, which is the position of the ith voxel. For N_v voxels, $\mathbf{C}^{(k)}$ is a $2N_v \times 2N_v$ block-diagonal matrix; the ith block being

$$\mathbf{F}_i^{(k)} = f^{(k)}(\boldsymbol{r}_i) \begin{pmatrix} \cos\phi^{(k)}(\boldsymbol{r}_i) & -\sin\phi^{(k)}(\boldsymbol{r}_i) \\ \sin\phi^{(k)}(\boldsymbol{r}_i) & \cos\phi^{(k)}(\boldsymbol{r}_i) \end{pmatrix} = \begin{pmatrix} \frac{\boldsymbol{B}_p^{(k)}(\boldsymbol{r}_i)\cdot\boldsymbol{e}_x}{B_p} & -\frac{\boldsymbol{B}_p^{(k)}(\boldsymbol{r}_i)\cdot\boldsymbol{e}_y}{B_p} \\ \frac{\boldsymbol{B}_p^{(k)}(\boldsymbol{r}_i)\cdot\boldsymbol{e}_y}{B_p} & \frac{\boldsymbol{B}_p^{(k)}(\boldsymbol{r}_i)\cdot\boldsymbol{e}_x}{B_p} \end{pmatrix}, \tag{9}$$

where

$$\cos\phi^{(k)}(\boldsymbol{r}_i) = \frac{\boldsymbol{B}_p^{(k)}(\boldsymbol{r}_i)\cdot\boldsymbol{e}_x}{\left\|\boldsymbol{B}_p^{(k)}(\boldsymbol{r}_i)\right\|_{xy}} \tag{10}$$

and

$$\sin\phi^{(k)}(\boldsymbol{r}_i) = \frac{\boldsymbol{B}_p^{(k)}(\boldsymbol{r}_i)\cdot\boldsymbol{e}_y}{\left\|\boldsymbol{B}_p^{(k)}(\boldsymbol{r}_i)\right\|_{xy}} \tag{11}$$

define the angle between $\boldsymbol{B}_p = B_p\boldsymbol{e}_x$ and $\boldsymbol{B}_p^{(k)}(\boldsymbol{r}_i)$, $\|\cdot\|_{xy}$ is the Euclidean norm of the x and y components of the argument, and

$$f^{(k)}(\boldsymbol{r}_i) = \frac{\left\|\boldsymbol{B}_p^{(k)}(\boldsymbol{r}_i)\right\|_{xy}}{B_p} \tag{12}$$

defines the change in the amplitude. If $\left\|\boldsymbol{B}_p^{(k)}(\boldsymbol{r}_i)\right\|_{xy} = 0$, the angle $\phi^{(k)}(\boldsymbol{r}_i)$ is undetermined; however, the final form of Eq. (9) is still valid.

In Appendix A, it is argued that the linear independence of the polarizing fields is a necessary and sufficient condition to produce linearly independent virtual sensors.

3. Methods

The proposed method was tested by ULF-MRI simulations using the geometry of the 304-channel SQUID system of Physikalisch-Technische Bundesanstalt in Berlin [9]. All the SQUID sensors are magnetometers; they are positioned inside a flat-bottom dewar and arranged in eight horizontal planes. The sensor array is 244 mm in diameter. The lowest and highest planes are 29 and 169 mm above the dewar bottom, respectively. The pick-up areas of the sensors are octagons with maximum diameter 7.2 mm. Further details of the sensor configuration can be found in [18].

We simulated a two-dimensional phantom positioned 40 mm below the lowest SQUID plane; center of the phantom was on the center axis of the dewar. The simulated phantom was constructed from the normal brain data of BrainWeb [19,20], with 1-mm resolution. For this study, 10 transverse planes from the middle of the data set were used. Neighboring voxels of the planes were merged to produce larger voxels, though preserving the original tissue types; for each large voxel, the tissue type that dominated in the merged voxels was chosen. Fig. 1a shows a visualization of the simulated phantom. The phantom had 15×15 voxels, with dimensions 12.1, 10.0, and 14.5 mm in the x, y, and z directions, respectively. Parameters of different tissues are listed in Table 1. These parameters have also been used for high-field MRI simulations [19,20]. However, according to [21–23], T_2 values do not depend strongly on the magnetic field strength; thus, the values are also suitable for ULF MRI.

Next, the simulation sequence is described (Fig. 2). Let us define the coordinates such that the origin is at the center of the lowest SQUID plane, $\boldsymbol{e}_y$ points upwards, and $\boldsymbol{e}_x$ and $\boldsymbol{e}_z$ define a plane parallel to the bottom of the dewar. The sample was first polarized to magnetic equilibrium using one of the polarizing fields $\boldsymbol{B}_p^{(k)}$, which are listed in Table 2 and illustrated in Fig. 1b. Then, $\boldsymbol{B}_p^{(k)}$ was switched off nonadiabatically and the measurement field
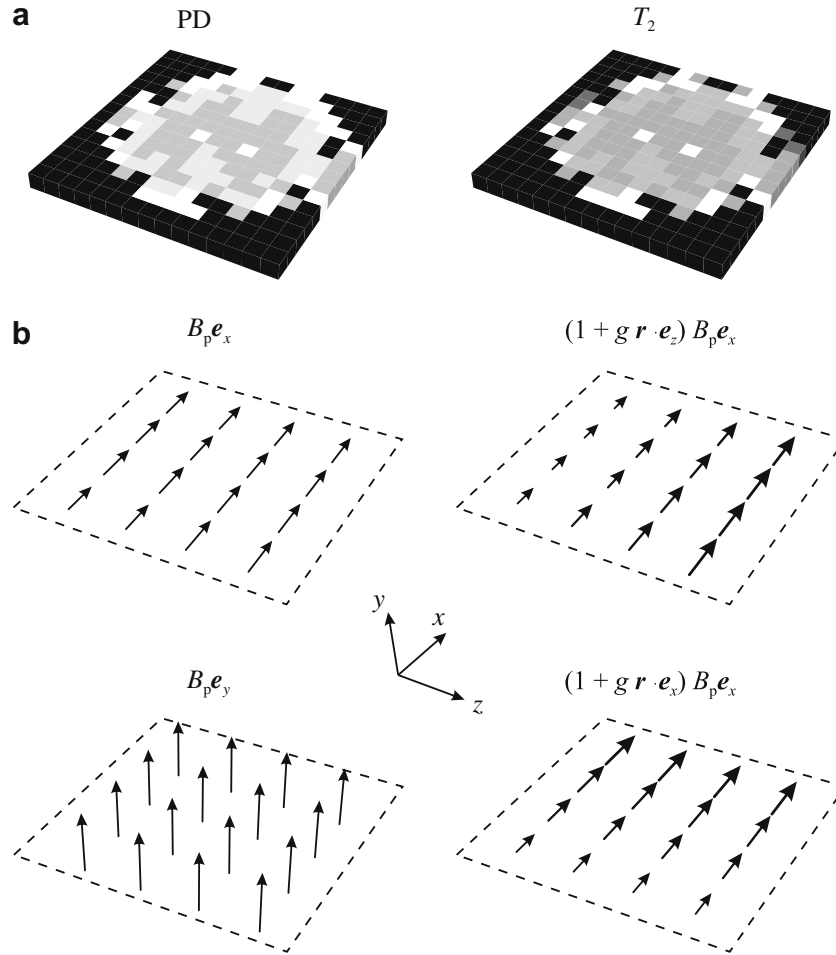
Fig. 1. (a) An illustration of the simulated phantom showing both the proton densities (PD) and T_2 times of the voxels. White color represents the maximum values of Table 1; voxels for which T_2 is undefined are printed black. (b) A schematic figure of the simulated polarizing fields that we used in this study, see Table 2. Arrow sizes are proportional to the field strengths. After the polarization periods, the simulation assumed a homogeneous measurement field along $\boldsymbol{e}_z$.

Table 1
Tissue parameters for the simulations. PD is proton density relative to that of cerebrospinal fluid.

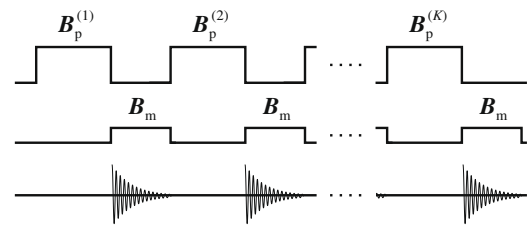| Tissue name	PD	T_2 (ms)
Background	0.00	–
Cerebrospinal fluid	1.00	329
Grey matter	0.86	83
White matter	0.77	70
Fat	1.00	70
Muscle/skin	1.00	47
Skin	1.00	329
Skull	0.00	–
Glial matter	0.86	83
Meat	0.77	70

Fig. 2. A schematic diagram of the simulated pulse sequence that we used to simulate polarization encoding. There are in total K different polarizing fields $\boldsymbol{B}_{\mathrm{p}}^{(k)}$. Each polarization period is followed by signal detection while the measurement field $\boldsymbol{B}_{\mathrm{m}}$ is applied.

$\boldsymbol{B}_{\mathrm{m}} = B_{\mathrm{m}}\boldsymbol{e}_z$, where $B_{\mathrm{m}} = 5$ µT, was applied. Simulated signals were sampled at 1 kHz while $\boldsymbol{B}_{\mathrm{m}}$ was on for 100 ms. This was repeated for the sets of $\boldsymbol{B}_{\mathrm{p}}^{(k)}$:s. The evaluation of the magnetization was simulated using the Bloch equations. Signals of the sensors were calculated by summing over the source phantom; for each voxel, the magnetization was assumed to be located at the center of the voxel. Finally, random white Gaussian noise, with standard deviation σ, was added to the signals.

For each of the cases (A–D, in Table 2), transverse components of the voxel magnetizations as a function of time were solved from Eq. (7) using the composite sensitivity matrix, its singular value

Table 2
Polarizing fields of the simulations. (A) One homogeneous field. (B) One homogeneous field and a field with a linear z-directional gradient; $g = 10$ m^{-1} defines the gradient strength. (C) Two orthogonal homogeneous fields. (D) Two orthogonal homogeneous fields and two fields with linear gradients in the x and z directions.

A	$\boldsymbol{B}_{\mathrm{p}}^{(1)} = B_{\mathrm{p}}\boldsymbol{e}_x$	
B	$\boldsymbol{B}_{\mathrm{p}}^{(1)} = B_{\mathrm{p}}\boldsymbol{e}_x$	$\boldsymbol{B}_{\mathrm{p}}^{(2)} = (1 + g\boldsymbol{r} \cdot \boldsymbol{e}_z)B_{\mathrm{p}}\boldsymbol{e}_x$
C	$\boldsymbol{B}_{\mathrm{p}}^{(1)} = B_{\mathrm{p}}\boldsymbol{e}_x$	$\boldsymbol{B}_{\mathrm{p}}^{(2)} = B_{\mathrm{p}}\boldsymbol{e}_y$
D	$\boldsymbol{B}_{\mathrm{p}}^{(1)} = B_{\mathrm{p}}\boldsymbol{e}_x$	$\boldsymbol{B}_{\mathrm{p}}^{(2)} = (1 + g\boldsymbol{r} \cdot \boldsymbol{e}_z)B_{\mathrm{p}}\boldsymbol{e}_x$
	$\boldsymbol{B}_{\mathrm{p}}^{(3)} = B_{\mathrm{p}}\boldsymbol{e}_y$	$\boldsymbol{B}_{\mathrm{p}}^{(4)} = (1 + g\boldsymbol{r} \cdot \boldsymbol{e}_x)B_{\mathrm{p}}\boldsymbol{e}_x$

decomposition, and by truncating singular values smaller than w_t to zero. w_t was chosen independently for each simulated noise level and polarization set such that mean errors over 10 simulations would have been larger with truncation values $w'_t = 3w_t/2$ and $w'_t = w_t/2$. Different truncation values were used when estimating the amplitudes and the T_2 times of the voxels. The transverse components were combined to create complex magnetizations. The magnetization of each voxel precesses around $\boldsymbol{B}_m$ and decays according to a tissue-specific relaxation time. Thus, for each voxel, a decaying complex sinusoidal function was fitted in the time domain using the HTLS (Hankel total least squares) method [24]. Estimates for the initial amplitudes and the T_2 relaxation times of the voxels were obtained from the fit parameters; prior knowledge of the polarizing field orientations was used to eliminate non-physical magnetization components.

Errors in the amplitude estimates were analyzed using the function

$$E_{amp} = \frac{\|\hat{\boldsymbol{m}}(0) - \boldsymbol{m}(0)\|_1}{\|\boldsymbol{m}(0)\|_1}, \tag{13}$$

where $\boldsymbol{m}$ and $\hat{\boldsymbol{m}}$ are the magnetization used for simulations and the estimated magnetization, respectively, and $\|\cdot\|_1$ is the l_1 norm. Similarly, errors in the estimated T_2 times were studied using the function

$$E_{T_2} = \frac{1}{N_{T_2}} \sum_{i=1}^{N_{T_2}} \frac{|\hat{T}_2(\boldsymbol{r}_i) - T_2(\boldsymbol{r}_i)|}{T_2(\boldsymbol{r}_i)}, \tag{14}$$

where the summation goes over the N_{T_2} voxels for which the T_2 time is defined and T_2 and $\hat{T}_2$ are the transverse relaxation times used for the simulations and its estimate, respectively.

4. Results

In the following, simulated results for the phantom (see Fig. 1a) are considered. Mean errors E_{amp} (Eq. 13) and E_{T_2} (Eq. 14) for 10 simulations are plotted in Figs. 3 and 4, respectively; the shaded region shows values that are at most one standard deviation away from the mean. Values of the horizontal axes are defined through

$$\lambda = \frac{B_p \sqrt{N_p}}{\sigma}, \tag{15}$$

where B_p is the amplitude of the polarizing field, N_p is the number of different polarizations used, and σ is the standard deviation of

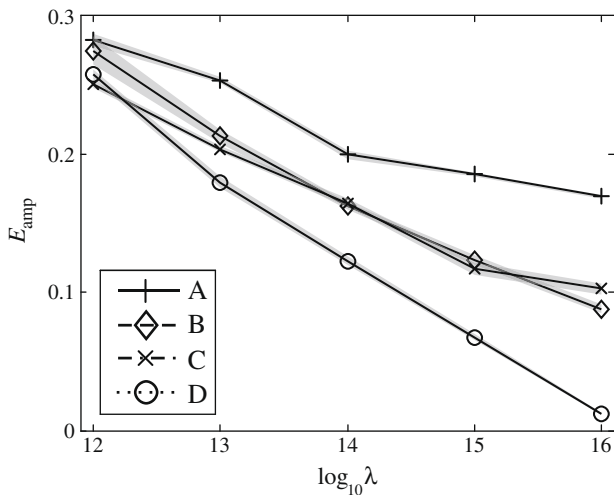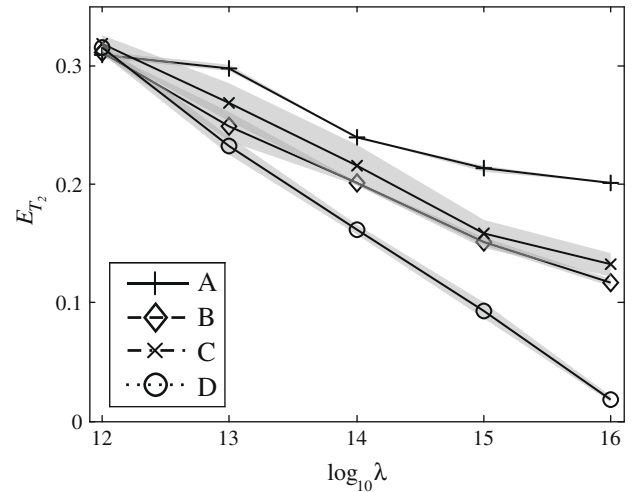**Fig. 4.** Averages of errors (Eq. 14) for 10 simulations with the simulated phantom; shaded regions show the mean ± one standard deviation. λ is defined in Eq. (15); characters A–D refer to different polarization sets, as explained in Table 2.

the noise. The factor $\sqrt{N_p}$ in λ makes the results of different N_p easily comparable; it is needed to scale the noise level, because in Eq. (7) the size of $\boldsymbol{s}'$ depends on N_p. For example, an increase in $\log_{10}\lambda$ by 1 can be interpreted as an order-of-magnitude increase of the polarizing fields.

Figs. 3 and 4 show that polarization encoding improves the estimation accuracy; if the aim is to obtain images with a given accuracy, polarization encoding can be used to reduce imaging times. In Fig. 5, the singular values of the composite sensitivity matrices are plotted. The figure shows that polarization encoding reduces the condition number of the sensitivity matrix, leading to more robust solutions. Moreover, with only one polarizing field it is impossible to produce precise images, even at high signal-to-noise ratio, because the sensitivity matrix is rank-deficient, i.e. there is not enough information to solve all the unknowns.

5. Discussion and conclusions

We propose a new way of encoding spatial information in magnetic resonance imaging. The method appears to be particularly
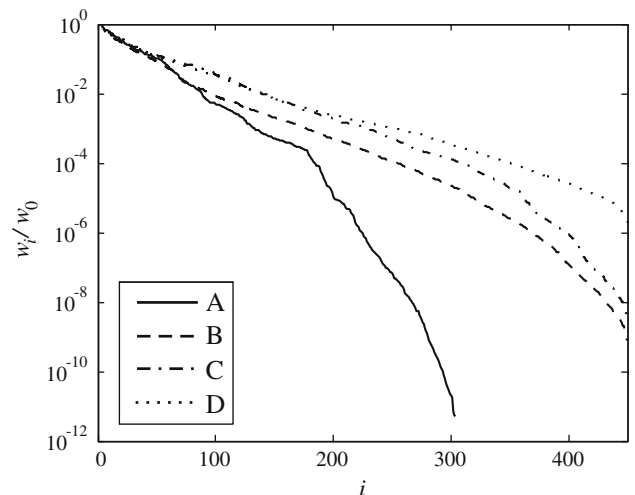

Fig. 3. Averages of errors (Eq. 13) for 10 simulations with the simulated phantom; shaded regions show the mean ± one standard deviation. λ is defined in Eq. (15); characters A–D refer to different polarization sets, as explained in Table 2.

Fig. 5. Non-zero singular values w_i of the composite sensitivity matrices $\boldsymbol{A}'$ for the simulated phantom with 15×15 voxels. Values are arranged in descending order, such that w_0 is the largest singular value. Characters A–D refer to the polarizations as listed in Table 2.

applicable to ultra-low-field MRI. It is conceptually based on the idea to impress a variety of polarization profiles to the object. With an adequate choice of such profiles, the image can be reconstructed from a series of measurements by the corresponding inverse transformation. In practice, the fields should be chosen, e.g. on the basis of instrumentation issues and the condition number of the composite sensitivity matrix $\boldsymbol{A}'$. The methods of this paper can be used to analyze also RF encoding, because it is only another way to produce magnetization profiles. For simplicity, we considered only sensors sensitive to the x and y components of the magnetization, which is enough for most purposes of MRI; still, the methods of this study can be easily generalized to produce virtual sensors with continuous sensitivities or virtual sensors that are sensitive to all three components of the magnetization.

In this study, we demonstrated the applicability of polarization encoding with simple polarizing field patterns. The benefits of the method depend on the shapes of the fields one is able to produce; when the fields are highly similar, the method resembles signal averaging with a single polarizing field. In general, it may be difficult to produce large images with small voxels by only using polarization encoding, because of the requirement $N_s N_p \geqslant 2N_v$. However, it is possible to combine the method with other encoding methods; for instance, one dimension can be encoded by polarization encoding and the others by Fourier encoding techniques. Then, a feasible number of parameters has to be solved using matrix inversions. Moreover, by careful coil design, it is possible to construct polarizing field profiles that are, approximately, from a certain function basis, e.g. wavelets or Fourier basis. Then, the inverse problem can be solved with well-behaving function transforms. In such cases, the method resembles SMASH, in which sensor arrays are designed such that the sensitivity profiles are spatial harmonics [5].

It has been demonstrated recently that the longitudinal proton polarization of a water flow can be measured by atomic magnetometers in the absence of precession [25]. Utilizing the frequency-independent broad-band sensitivity of SQUIDs, it may even be possible to measure directly the relaxation of the longitudinal magnetization of a static sample. Similar to what was shown for the relaxation of magnetic nanoparticles in an animal model by moving a sensor with respect to the sample [26] or by using a large sensor array [27], this may end up in a new kind of magnetic imaging by using polarization encoding in addition to established reconstruction techniques.

The proposed method is especially suitable for ULF MRI, because at low fields it is possible to construct sets of polarizing fields. Moreover, at low fields, imaging processes need improvements because current methods are slow and suffer from poor image quality. Although pMRI methods reduce imaging times in ULF MRI [14], there is always a need for the prepolarization. Polarization encoding utilizes the otherwise suboptimally used prepolarization time for signal encoding.

Acknowledgment

Appendix A. Requirements for the polarizing fields

In the following, it will be shown that the linear independence of the polarizing fields is a sufficient condition to produce linearly independent virtual sensors. First, assume there is a linearly independent set $\mathscr{B}$ of polarizing fields:

$$\mathscr{B} = \left\{ \boldsymbol{B}_p^{(k)} | k = 1, \cdots, K \right\} \tag{16}$$

such that, for all k, there exist no coefficients c_j for which

$$\boldsymbol{B}_{p-xy}^{(k)} = \sum_{\substack{j=1, j \neq k}}^{K} c_j \boldsymbol{B}_{p-xy}^{(j)}, \tag{17}$$

where

$$\boldsymbol{B}_{p-xy}^{(k)} = \left(\boldsymbol{B}_p^{(k)} \cdot \boldsymbol{e}_x, \boldsymbol{B}_p^{(k)} \cdot \boldsymbol{e}_y \right)^{\mathrm{T}}. \tag{18}$$

As was shown in Section 2, these polarizing fields can be used to produce virtual sensors. Next, it will be shown that for each physical sensor that is sensitive to all source voxels, a linearly independent set of K virtual sensors can be created using the set $\mathscr{B}$.

Consider the lth physical sensor, whose sensitivity is described by the lth row of $\boldsymbol{A}$ in Eq. (3). The respective virtual sensors are defined by the lth rows of $\boldsymbol{AC}^{(k)}$:s, where the blocks of $\boldsymbol{C}^{(k)}$ are given by Eq. (9). The $(2i-1)$th and $(2i)$th elements of the lth row of $\boldsymbol{AC}^{(k)}$ for $i = 1, \cdots, N_v$ are

$$\begin{pmatrix} (\boldsymbol{AC}^{(k)})_{l,2i-1} \\ (\boldsymbol{AC}^{(k)})_{l,2i} \end{pmatrix} = \begin{pmatrix} A_{l,2i-1} & A_{l,2i} \\ A_{l,2i} & -A_{l,2i-1} \end{pmatrix} \frac{\boldsymbol{B}_{p-xy}^{(k)}(\boldsymbol{r}_i)}{B_p}, \tag{19}$$

where the subscripts of A refer to the elements of $\boldsymbol{A}$. Assume that the sensitivity of the kth virtual sensor can be written as a linear combination of the sensitivities of the other virtual sensors:

$$\begin{pmatrix} (\boldsymbol{AC}^{(k)})_{l,2i-1} \\ (\boldsymbol{AC}^{(k)})_{l,2i} \end{pmatrix} = \sum_{\substack{j=1, j \neq k}}^{K} c_j \begin{pmatrix} (\boldsymbol{AC}^{(j)})_{l,2i-1} \\ (\boldsymbol{AC}^{(j)})_{l,2i} \end{pmatrix} = \begin{pmatrix} A_{l,2i-1} & A_{l,2i} \\ A_{l,2i} & -A_{l,2i-1} \end{pmatrix} \sum_{\substack{j=1, j \neq k}}^{K} c_j \frac{\boldsymbol{B}_{p-xy}^{(j)}(\boldsymbol{r}_i)}{B_p}. \tag{20}$$

Since the lth coil is sensitive to all voxels, i.e. at least $A_{l,2i-1} \neq 0$ or $A_{l,2i} \neq 0$ for $i = 1, \cdots, N_v$, Eqs. (19 and 20) yield

$$\boldsymbol{B}_{p-xy}^{(k)} = \sum_{\substack{j=1, j \neq k}}^{K} c_j \boldsymbol{B}_{p-xy}^{(j)}. \tag{21}$$

Because the assumption of linearly dependent virtual sensors implies linearly dependent polarizing fields, linearly independent polarizing fields produce independent virtual sensors. For notational simplicity, sensors were assumed to be sensitive to all voxels. However, if a sensor is sensitive to only a subset of all voxels, it can be proved similarly as above that the linear independence of the polarizing fields is required in the region defined by the subset.

In addition, it is simple to prove that when adding linearly dependent polarizing fields to an existing field set, no new information is gained. Thus, the linear independence of the polarizing fields is a necessary and sufficient condition to produce linearly independent virtual sensors.

References

[1] P.C. Lauterbur, Image formation by induced local interactions: examples employing nuclear magnetic resonance, Nature 242 (1973) 190–191.

[2] Z.H. Cho, O. Nalcioglu, H.W. Park, Methods and algorithms for Fourier-transform nuclear magnetic resonance tomography, J. Opt. Soc. Am. A 4 (1987) 923–932.

[3] J.B. Weaver, Y. Xu, D.M. Healy, J.R. Driscoll, Wavelet-encoded MR imaging, Magn. Reson. Med. 24 (1992) 275–287.

[4] G.P. Zientara, L.P. Panych, F.A. Jolesz, Dynamically adaptive MRI with encoding by singular value decomposition, Magn. Reson. Med. 32 (1994) 268–274.

[5] D.K. Sodickson, W.J. Manning, Simultaneous acquisition of spatial harmonics (SMASH): fast imaging with radiofrequency coil arrays, Magn. Reson. Med. 38 (1997) 591–603.

[6] K.P. Pruessmann, M. Weiger, M.B. Scheidegger, P. Boesiger, SENSE: Sensitivity encoding for fast MRI, Magn. Reson. Med. 42 (1999) 952–962.

[7] M.A. Griswold, P.M. Jakob, R.M. Heidemann, M. Nittka, V. Jellus, J. Wang, B. Kiefer, A. Haase, Generalized autocalibrating partially parallel acquisitions (GRAPPA), Magn. Reson. Med. 47 (2002) 1202–1210.

[8] R. McDermott, S.K. Lee, B. ten Haken, A.H. Trabesinger, A. Pines, J. Clarke, Microtesla MRI with a superconducting quantum interference device, PNAS 101 (2004) 7857–7861.

[9] M. Burghoff, S. Hartwig, W. Kilian, A. Vorwerk, L. Trahms, SQUID systems adapted to record nuclear magnetism in low magnetic fields, IEEE Trans. Appl. Supercond. 17 (2007) 846–849.

[10] V.S. Zotev, A.N. Matlachov, P.L. Volegov, H.J. Sandin, M.A. Espy, J.C. Mosher, A.V. Urbaitis, S.G. Newman, R.H. Kraus Jr., Multi-channel SQUID system for MEG and ultra-low-field MRI, IEEE Trans. Appl. Supercond. 17 (2007) 839–842.

[11] M. Pannetier, C. Fermon, G. Le Goff, J. Simola, E. Kerr, Femtotesla magnetic field measurement with magnetoresistive sensors, Science 304 (2004) 1648–1650.

[12] M. Pannetier-Lecoeur, C. Fermon, N. Biziere, J. Scola, A.L. Walliang, RF response of superconducting-GMR mixed sensors, application to NQR, IEEE Trans. Appl. Supercond. 17 (2007) 598–601.

[13] I.M. Savukov, V.S. Zotev, P.L. Volegov, M.A. Espy, A.N. Matlashov, J.J. Gomez, R.H. Kraus Jr., MRI with an atomic magnetometer suitable for practical imaging applications, J. Magn. Reson. 199 (2009) 188–191.

[14] V.S. Zotev, P.L. Volegov, A.N. Matlashov, M.A. Espy, J.C. Mosher, R.H. Kraus Jr., Parallel MRI at microtesla fields, J. Magn. Reson. 192 (2008) 197–208.

[15] J. Nieminen, Polarization encoding for magnetic resonance imaging, Master's thesis, Helsinki University of Technology, 2008.

[16] J.O. Nieminen, M. Burghoff, L. Trahms, R.J. Ilmoniemi, Magnetic resonance imaging using sensor arrays of SQUIDs and by polarization encoding, in: Book of Abstracts, 16th International Conference on Biomagnetism, Biomag 2008, August 25–29, 2008, Sapporo, Japan, pp. 189–190.

[17] F. Bloch, Nuclear induction, Phys. Rev. 70 (1946) 460–474.

[18] A. Schnabel, M. Burghoff, S. Hartwig, F. Petsche, U. Steinhoff, D. Drung, H. Koch, A sensor configuration for a 304 SQUID vector magnetometer, Neurol. Clin. Neurophysiol. 70 (2004).

[19] D.L. Collins, A.P. Zijdenbos, V. Kollokian, J.G. Sled, N.J. Kabani, C.J. Holmes, A.C. Evans, Design and construction of a realistic digital brain phantom, IEEE Trans. Med. Imaging 17 (1998) 463–468.

[20] http://www.bic.mni.mcgill.ca/brainweb/, May 11, 2009.

[21] V.S. Zotev, A.N. Matlashov, P.L. Volegov, I.M. Savukov, M.A. Espy, J.C. Mosher, J.J. Gomez, R.H. Kraus Jr., Microtesla MRI of the human brain combined with MEG, J. Magn. Reson. 194 (2008) 115–120.

[22] P.A. Bottomley, C.J. Hardy, R.E. Argersinger, G. Allen-Moore, A review of ^{1}H nuclear magnetic resonance relaxation in pathology: are T_1 and T_2 diagnostic?, Med Phys. 14 (1987) 1–37.

[23] J.P. Wansapura, S.K. Holland, R.S. Dunn, W.S. Ball Jr., NMR relaxation times in the human brain at 3.0 tesla, J. Magn. Reson. Imaging 9 (1999) 531–538.

[24] S. Vanhuffel, H. Chen, C. Decanniere, P. Vanhecke, Algorithm for time-domain NMR data fitting based on total least squares, J. Magn. Res. A 110 (1994) 228–237.

[25] C.W. Crawford, S. Xu, E.J. Siegel, D. Budker, A. Pines, Fluid-flow characterization with nuclear spins without magnetic resonance, Appl. Phys. Lett. 93 (2008) 092507.

[26] E. Romanus, M. Hückel, C. Groß, S. Prass, W. Weitschies, R. Bräuer, P. Weber, Magnetic nanoparticle relaxation measurement as a novel tool for in vivo diagnostics, J. Magn. Magn. Mater. 252 (2002) 387–389.

[27] R. Jurgons, C. Seliger, A. Hilpert, L. Trahms, S. Odenbach, C. Alexiou, Drug loaded magnetic nanoparticles for cancer therapy, J. Phys. Cond. Matter 18 (2006) S2893–S2902.